46

Crystal Growth, Density Functional Theory, and Scintillation Properties 1 2 $Tl_3LnCl_6:Ce^{3+}$ and $TlLn_2Cl_7:Ce^{3+}$ (Ln = Y, Gd) 3 4 Edgar van Loef,^{1,*} Urmila Shirwadkar,¹ Lakshmi Soundara Pandian,¹ Guido Ciampi,¹ Luis 5 Stand, Mao-Hua Du, Merry Koschan, Matthew Loyd, Mariya Zhuravleva, A Charles Melcher, 6 7 4,5 Kanai Shah 1 8 9 ¹ Radiation Monitoring Devices Inc., 44 Hunt Street, Watertown, MA 02472, USA 10 ² Scintillation Materials Research Center, University of Tennessee, Knoxville, Knoxville, TN 37996, USA 11 ³ Oak Ridge National Laboratory, Oak Ridge, TN 37831, USA 12 13 ⁴ Department of Materials Science and Engineering, University of Tennessee, Knoxville, 14 Knoxville, TN 37996, USA 15 ⁵ Department of Nuclear Engineering, University of Tennessee, Knoxville, Knoxville, TN 37996, 16 **USA** 17 18 *Corresponding author: E. V. van Loef 19 E-mail: EvanLoef@RMDInc.com Address: Radiation Monitoring Devices, Inc. (RMD), 44 Hunt Street, Watertown, MA 02472, 20 21 **USA** 22 Tel.: +1 (617) 668 6984 23 Fax: +1 (617) 926 9980 24 25 26 27 28 29 30 31 32 33 34 35 36 37 38 39 This manuscript has been co-authored by UT-Battelle, LLC under Contract No. DE-AC05-00OR22725 with the 40 U.S. Department of Energy. The United States Government retains and the publisher, by accepting the article 41 for publication, acknowledges that the United States Government retains a non-exclusive, paid-up, irrevocable, 42 world-wide license to publish or reproduce the published form of this manuscript, or allow others to do so, for 43 United States Government purposes. The Department of Energy will provide public access to these results of 44 research with the DOE federally sponsored in accordance Public Access Plan 45 (http://energy.gov/downloads/doe-public-access-plan).

ABSTRACT

In this paper we report on the crystal growth, density functional theory (DFT) calculations and scintillation properties of Tl₃LnCl₆:Ce³⁺ and TlLn₂Cl₇:Ce³⁺ (Ln = Y, Gd). Crystals were grown by the Vertical Bridgman technique up to 16 mm in diameter and 25 mm long. Crystals of Tl₃YCl₆:Ce³⁺ and Tl₃GdCl₆:Ce³⁺ belong to the family of the *Nesohalides* which have the monoclinic crystal structure. Crystals of TlY₂Cl₇:Ce³⁺ and TlGd₂Cl₇:Ce³⁺ belong to the family of the *Phyllohalides* which have either the monoclinic or the orthorhombic crystal structure. The light yields of these *Nesohalides* and *Phyllohalides* are typically on the order of 35,000 – 40,000 ph/MeV.

Keywords: Inorganic scintillators; Thallium-based scintillators; Radiation detectors; Gamma-ray spectroscopy; DFT calculations.

1. INTRODUCTION

The last decade has seen remarkable advances in the detection of ionizing radiation using inorganic scintillators. Ce-doped halides such as LaBr₃ and Cs₂LiLa(Br,Cl)₆ have broken through the 3% energy resolution barrier, rivaling semiconductor radiation detectors and delivering a more accurate detection of special nuclear materials. On the other hand, isotope identification in mixed neutron/gamma radiation fields has benefited tremendously from dual-mode scintillators such as Cs₂LiYCl₆ and Cs₂LiLa(Br,Cl)₆ which have replaced expensive He-3 detectors. The only significant drawback is that the detection efficiency for gamma-rays is still relatively low for Cedoped halide scintillators, primarily because they contain very few high-Z constituents (limiting their effective Z to < 50 and density to < 5 g/cm³).

Recently, however, research has been initiated to address this shortfall where the focus is to replace lighter ions of Ce-doped halide scintillators with isovalent heavier ones (e.g. Cs, Rb, or K replaced with Tl) and observing the effects on the density, effective Z and scintillation properties of the Tl-analogs of the original Ce-doped halide scintillators.

In this paper we report on the crystal growth, density functional theory (DFT) calculations and scintillation properties of $Tl_3LnCl_6:Ce^{3+}$ and $TlLn_2Cl_7:Ce^{3+}$ (Ln = Y, Gd). X-Ray diffraction, thermodynamic properties such as moisture absorption, radioluminescence, and scintillation properties such as light yield and scintillation decay time spectra are presented.

2. EXPERIMENTAL SECTION

2.1 Crystal Growth

Single crystals of Tl₃LnCl₆ and TlLn₂Cl₇ (Ln = Y, Gd) doped with different Ce³⁺ concentrations were grown by the Vertical Bridgman method in sealed quartz ampoules (Ø 16 mm) using single zone furnaces. Anhydrous beads of thallium chloride, together with the yttrium chloride or gadolinium chloride, and a small amount of cerium chloride were loaded in the appropriate stoichiometric ratio into quartz ampoules which were subsequently sealed under reduced pressure. Crystals were typically grown at a rate of 10 mm/day from the top to the bottom



Figure 1. Photographs of $Tl_3YCl_6:Ce^{3+}$ (top) and $TlY_2Cl_7:Ce^{3+}$ (bottom) crystals grown at RMD.



Figure 2. Photographs of Tl₃GdCl₆:Ce³⁺ (top) and TlGd₂Cl₇:Ce³⁺ (bottom) crystals grown at RMD.

in the gradient of the Bridgman furnace. After the crystal growth was finished, the furnace was cooled to room temperature at a rate of 10 °C/hour. Crystal thus obtained were typically 2 cm³ or smaller. Photographs of some of the crystal boules grown at RMD are shown in Figure 1 and Figure 2.

According to the phase diagram of TlCl – GdCl₃ [1] two congruently melting compositions are formed: $TlGd_2Cl_7$ and Tl_3GdCl_6 , and one incongruently melting composition: Tl_2GdCl_5 . Of the two congruently melting compositions, it seems that Tl_3GdCl_6 may exhibit a phase change in the solid at 400 and 290°C. No phase diagram of TlCl – YCl₃ was found in literature. We assume however that it is very similar to that of the thallium – gadolinium chloride. Crystals of $TlY_2Cl_7:Ce^{3+}$ and $TlGd_2Cl_7:Ce^{3+}$ grow congruently and do not appear to have any parasitic phase change between room temperature and their melting points. However, crystals of $TlY_2Cl_7:Ce^{3+}$ and $TlGd_2Cl_7:Ce^{3+}$ are somewhat hazy and form striations during cooling which we attribute to their layered crystal structure. Crystals of $Tl_3YCl_6:Ce^{3+}$ and $Tl_3GdCl_6:Ce^{3+}$ are hazy as well and appear to be polycrystalline, possibly due to the aforementioned phase change.

2.2 Thermodynamic Properties

The hygroscopicity of each sample was determined using a Surface Measurement Systems Dynamic Vapor Sorption (DVS) instrument. In this instrument, samples are placed on a sample tray suspended from a high-precision balance inside of a temperature and humidity-controlled atmosphere, and the weight is continuously monitored. The samples measured included a 10 to 15 mg piece of each composition plus a NaI:Tl sample, all with similar geometries for better comparison. Each sample in turn was placed on an aluminum sample tray and hung on the balance, and the DVS was set at 25°C and 40% relative humidity for 1000 minutes. The percent mass change vs time was plotted.

The thermal properties of each composition were analyzed using a Seteram Labsys Evo differential scanning calorimetry (DSC) instrument. Due to the volatility and toxicity of the materials, the samples were vacuum sealed inside quartz crucibles prior to measurement. The benefits of this method versus standard alumina crucibles have been discussed in depth [2]. The DSC furnace was heated and cooled at a rate of 5 K per minute. The heating and cooling rate used is considered to be typical for this type of measurement and is not expected to contribute to supercooling. Note that these analyses were only performed on the TlLn₂Cl₇ crystals due to the low quality of the Tl₃LnCl₆ samples.

2.3 Powder X-Ray Diffraction

High-resolution powder X-ray diffraction (XRD) was used for phase analysis and derivation of the lattice constants. Due to the hygroscopic nature of the materials measured, sample preparation was carried out inside of a nitrogen-purged glovebox unless otherwise noted. Samples for XRD were taken from the grown crystal and ground using a mortar and pestle. The powdered samples were loaded onto a Si zero-background sample stage and covered with a Kapton film for protection during measurement. The sample stage was then removed from the glovebox and placed into a PANalytical Empyrean 2-theta Diffractometer. The X-rays were generated with a Cu X-ray tube operated at 45 kV and 40 mA. Scans were taken in the range of 10-70 ° 2-theta with a step size of 0.0131 ° and a step time of 39.5 s.

HighScore software was used to compare the measured patterns with published structures [3]. Determination of the lattice parameters was carried out using GSAS-II, an open-source software package for Rietveld refinement [4]. No published structures were found for TlY₂Cl₇ and TlGd₂Cl₇, but their peaks matched well with those of InY₂Cl₇, which was used as the structure for refinement with Tl substituted for In [5].

2.4. Computational Methods

Theoretical calculations were performed on Tl₃YCl₆, Tl₃GdCl₆, TlY₂Cl₇ and TlGd₂Cl₇ using density functional theory (DFT) as implemented in the VASP code [6]. The interaction between ions and electrons is described by the projector augmented wave method [7]. Lattice parameters as well as atomic positions were fully relaxed using the PBE functional [8]. Electronic structure and density of states (DOS) were also calculated at the PBE level. The atomic positions were further relaxed using the hybrid PBE0 functional [9] while keeping the PBE lattice parameters. The PBE band gap was also corrected by using the PBE0 functional. The use of the hybrid PBE0 functional, which includes 25% nonlocal Fock exchange, improves band gap calculations, especially for large-gap insulators [10, 11, 12], and provides a better description of charge localization [12, 13, 14, 15, 16] which is critically important to the calculation of highly localized Ce-4f electrons. For Ga compounds, we used a Gd pseudopotential with Gd-4f orbitals frozen in the core to reduce the computational cost [17, 18, 19], with this method, we focus on Ce emission and neglect effects of the Gd-4f states and the associated magnetic moment of Gd³⁺ on structures and electronic structure. The DFT-D3 van der Waals functional [20] was used in calculations for both compounds for their quasi-low-dimensional structures.

The ground- and excited-state structures of Ce-doped Tl compounds were obtained by hybrid PBE0 calculations. The occupation numbers of the electron-occupied Ce-5d and the hole-occupied Ce-4f eigenlevels were fixed ([Δ self-consistent field (Δ SCF) method [21, 22, 23]) for the total energy calculation of the excited-state of TlY₂Cl₇:Ce³⁺ and TlGd₂Cl₇:Ce³⁺. The Δ SCF method combined with the hybrid PBE0 functional allows for the accurate calculation of excited-state structural relaxation, and the emission energy can be calculated based on the relaxed excited-state structure following the Franck-Condon principle. The calculated emission energies in many compounds based on the above approach have shown excellent agreement with experimental results [24, 25, 26, 27, 28].

2.5 Scintillation Properties

Radioluminescence spectra were recorded at room temperature using a Philips X-ray tube with a Cu anode operated at 40 kV and 20 mA. Light was dispersed through a McPherson 234 monochromator equipped with a grating (600 grooves/mm, blazed at 500 nm) and detected with a Burle C31034 photomultiplier tube (PMT). The GaAs photocathode was cooled to -50°C using dry-ice in order to minimize dark counts. Spectra were measured in 1 nm increments and integrated for 1 sec per interval. Spectra were corrected for the spectral response of the system.

Scintillation properties such as energy resolution, light yield, and non-proportionality were measured using a super-bialkali (SBA) Hamamatsu photomultiplier tube (PMT) (model #R6233-100) and standard nuclear instrumentation modules from Canberra such as a preamplifier (model #2005), a spectroscopy amplifier (model #2022), an ADC (model #8075), and a MCA (model #8000D) from Amptek. Pulse height spectra were collected using a ¹³⁷Cs radiation source.

Crystals were tested in a mineral oil filled quartz container in order to protect the samples from moisture. Optical grease was used to couple the quartz cup to the PMT window. Light yields, expressed in photoelectrons per MeV (phe/MeV), were determined by comparing the peak position of the 662 keV full energy peak in the pulse height spectra with that of BGO. The absolute light yield, expressed as the number of photons per MeV (ph/MeV), was calculated from the number of photoelectrons per MeV by dividing this number by the quantum efficiency of the PMT.

Scintillation decay was measured by optically coupling the quartz container to a Hamamatsu PMT (model #H6610) operating at -2000V and irradiated with 511 keV gamma rays from a ²²Na source. A 1GHz digital oscilloscope from Teledyne LeCroy (model #HDO 6104) was connected

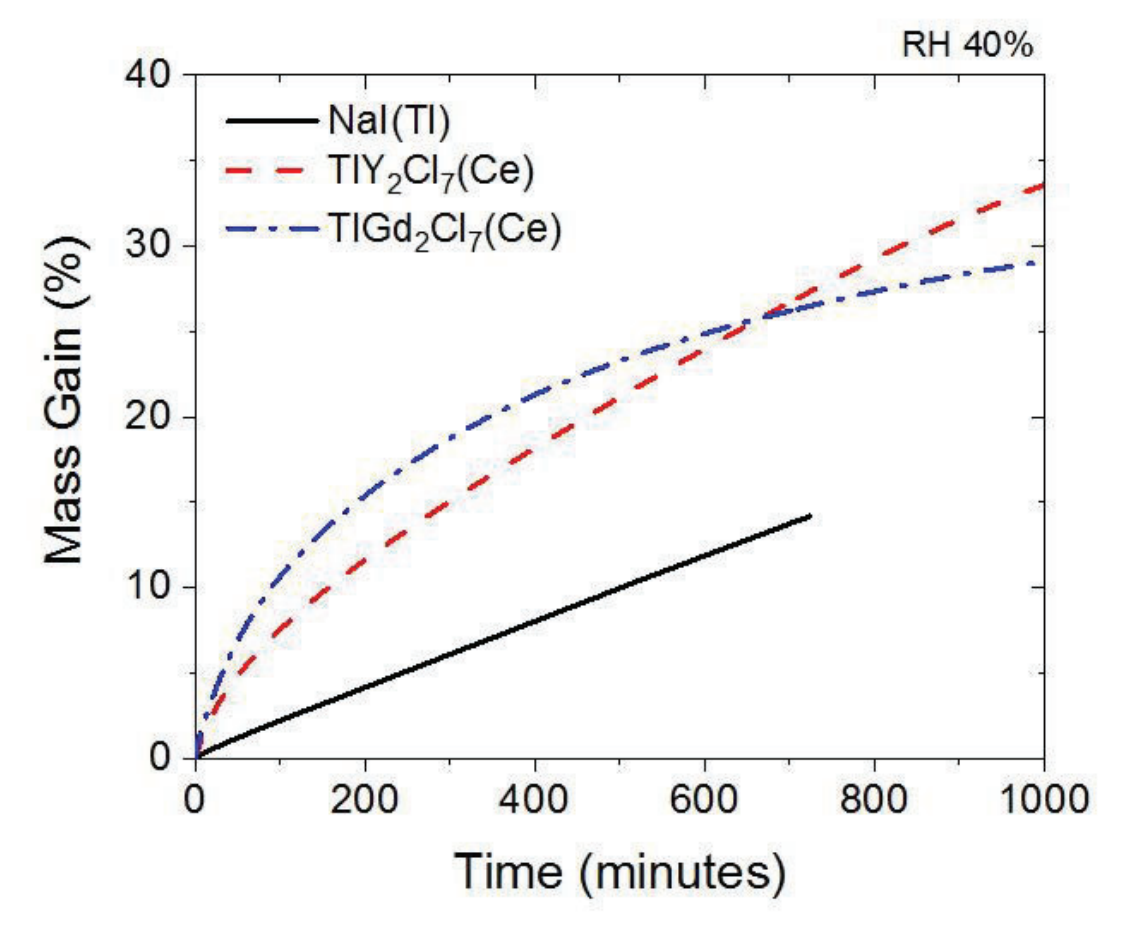


Figure 3. Mass gain plot of TlY₂Cl₇:Ce³⁺ and TlGd₂Cl₇:Ce³⁺, and NaI:Tl.

directly to the PMT anode to collect the data. In some cases, the PMT output was connected to a CAEN digitizer (12-bit, 250 MS/s). Timing measurements were done using a fast Hamamatsu PMT (rise time 0.7 ns) and a Teledyne Lecroy 1GHZ 12-bit resolution digital oscilloscope.

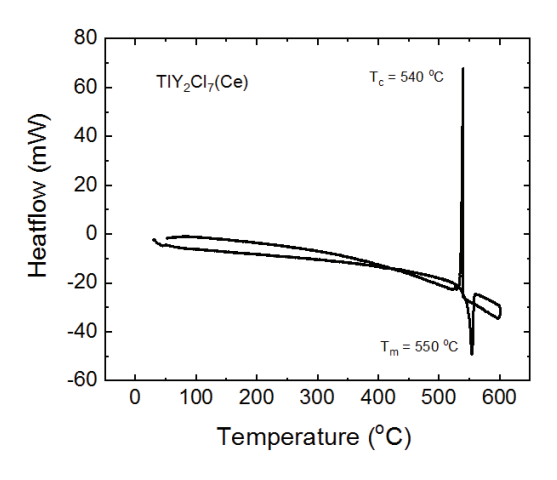
3. RESULTS AND DISCUSSION

3.1 Gravimetric and Thermal Analysis

Small samples of TlY₂Cl₇:Ce³⁺ and TlGd₂Cl₇:Ce³⁺, and NaI:Tl were measured using a DVS intrinsic instrument to compare their moisture absorption rates. The mass gain during the measurement is plotted in Figure 3.

TlY₂Cl₇:Ce³⁺ and TlGd₂Cl₇:Ce³⁺ gained 5% and 7% mass during the first hour, respectively. The mass gain of TlGd₂Cl₇:Ce³⁺ continued at a faster pace than TlY₂Cl₇:Ce³⁺ until after approximately 4 hours where the mass gain rate of TlGd₂Cl₇:Ce³⁺ slowed compared to that of TlY₂Cl₇:Ce³⁺. After 10 hours, each sample had gained about 25% mass. The mass gain of NaI:Tl is overall very linear and has a shallower slope compared to TlY₂Cl₇:Ce³⁺ and TlGd₂Cl₇:Ce³⁺.

DSC measurements of TlY₂Cl₇:Ce³⁺ and TlGd₂Cl₇:Ce³⁺ were carried out using sealed quartz ampoules, which allowed for a clean measurement without volatilization of the sample; however, the ampoules eliminated the possibility of thermal gravimetric analysis measurements.



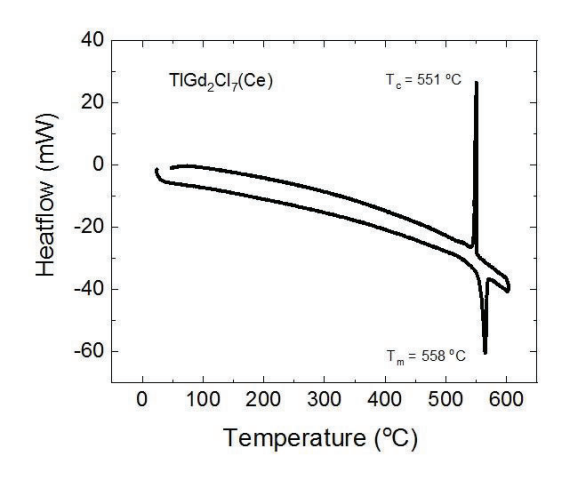


Figure 4. DSC curves of TlY₂Cl₇:Ce³⁺.

Figure 5. DSC curves of TlGd₂Cl₇:Ce³⁺.

The heat flow curves acquired for TlY₂Cl₇:Ce³⁺ and TlGd₂Cl₇:Ce³⁺ are plotted in Figure 4 and Figure 5, respectively. The melting points were measured to be 550 and 558°C, respectively. Both samples had single melting and crystallization peaks and no evidence of secondary phases. The degree of supercooling (separation between melting point and crystallization point) is about 7 – 10°C which is well within normal range.

3.2 Powder X-ray Diffraction

Powder diffraction patterns of TlY₂Cl₇:Ce³⁺ and TlGd₂Cl₇:Ce³⁺ measured at room temperature are plotted in Figure 6. The two compositions appear to be isostructural due to the similarities in their patterns, albeit with slightly different lattice parameters. The obtained patterns for the Tl₃LnCl₆:Ce³⁺ samples contained a number of unidentifiable peaks; therefore, their phase analysis could not be reliably performed.

Although there was no published structure for either TlLn₂Cl₇:Ce³⁺ compound, a search in HighScore revealed a match with the peaks of InY₂Cl₇. The structure of InY₂Cl₇ was used as the initial structure for Rietveld refinement of TlY₂Cl₇ by replacing the In atoms with Tl, and of TlGd₂Cl₇ by replacing the In atoms with Tl. The Ce³⁺ dopant was not considered when refining the structure but may have an effect on the lattice parameters when compared to an undoped crystal. Refinement was carried out with GSASII.

The intensities for hygroscopic metal halides are often in disagreement with their simulated patterns due to preferred orientation [29, 30]. Because of this, measurements such as single crystal diffraction must be carried out to further refine the atom positions (which affect the intensity of peaks).

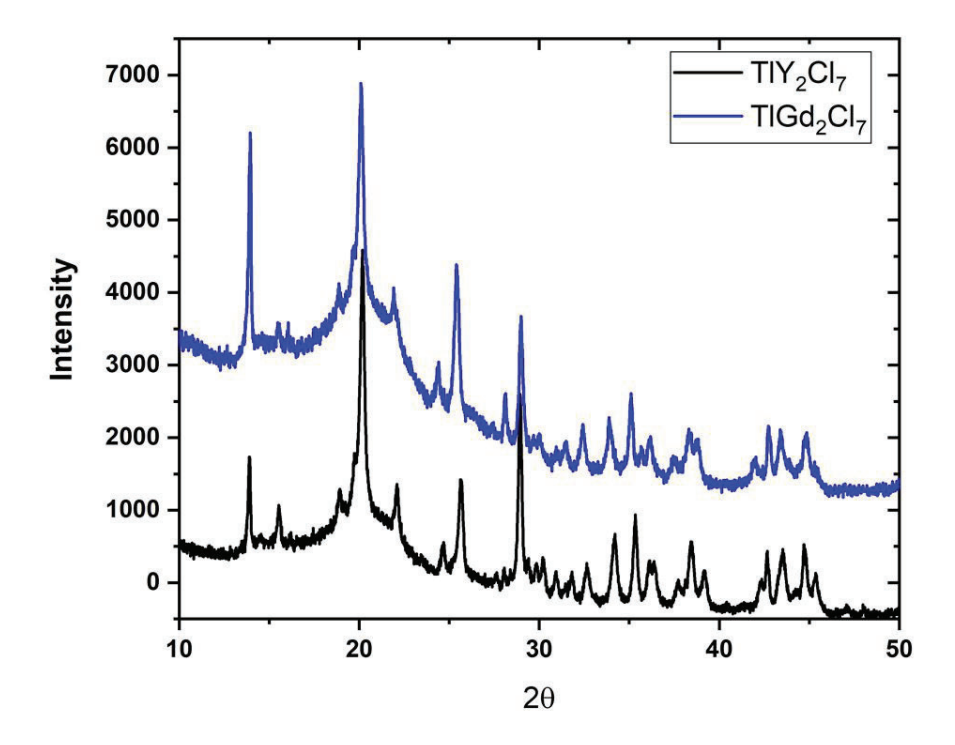


Figure 6. X-Ray powder diffraction patterns of TlY₂Cl₇:Ce³⁺ and TlGd₂Cl₇:Ce³⁺.

The crystallographic properties of $TIY_2Cl_7:Ce^{3+}$ and $TIGd_2Cl_7:Ce^{3+}$ are summarized in Table 1. Crystals of $TIY_2Cl_7:Ce^{3+}$ and $TIGd_2Cl_7:Ce^{3+}$ have the orthorhombic crystal structure with space group Pnma (62). Based on structure and lattice parameters, the calculated density of $TIY_2Cl_7:Ce^{3+}$ and $TIGd_2Cl_7:Ce^{3+}$ is 3.77 g/cm³ and 4.49 g/cm³, respectively. The effective Z is 60 and 64, respectively.

Table 1. Crystallographic properties of TlY₂Cl₇:Ce³⁺ and TlGd₂Cl₇:Ce³⁺.

	TIY ₂ CI ₇	TIGd ₂ Cl ₇
Density	3.77 g/cm ³	4.49 g/cm ³
$\mathbf{Z}_{\mathrm{eff}}$	60	64
Crystal structure	Orthorhombic	Orthorhombic
Space group	Pnma	Pnma
a (Å)	12.698(1)	12.690(2)
b (Å)	6.9107(7)	6.986(1)
C (Å)	12.671(1)	12.837(2)
α (°)	90.00	90.00
β (°)	90.00	90.00
γ (°)	90.00	90.00
Volume (ų)	1111.9(2)	1137.7(5)

3.3 Theoretical Modeling

222

223

224

225

226

227

228

229

230

231

232233

234

235

236

237

238

239

240

241

242

243

244

245

246

247248

249

250

251

252

253

254255

256

257

258

259

260

261

262263

264265

266267

TlY₂Cl₇ and TlGd₂Cl₇ have a layered, quasi-2D crystal structure as mentioned earlier. This plays a role in the electronic band structure as in such structures the electronhole pairs are usually more localized. Figure 7 shows the electronic band structure and DOS of TlY₂Cl₇ obtained by PBE calculations. The conduction band minimum (CBM) is at the Γ point while the valence band maximum (VBM) is located between the Γ and Z points. However, the top of the valence band at the Γ point is only slightly lower in energy than the VBM (by 0.02 eV). Thus, the band gap of TlY₂Cl₇ is nearly direct. The direct band gap at the Γ point is calculated to be 4.32 eV at the PBE level [Figure 7 (a)] which is expected to be underestimated due to the well-known PBE band gap error, and is corrected to be 6.41 eV by the hybrid functional PBE0 calculation. The conduction band is made up of both Tl-6p and Y-4d orbitals while the valance band has a predominantly Cl-3p character with some mixing of Tl-6s and Y-4d orbitals [Figure 7 (b)]. Since the Gd-4f orbitals are frozen in the core of the Gd pseudopotential, the calculated band structure and DOS of TlGd₂Cl₇ are similar to those of TlY₂Cl₇ except that Y-4d orbitals are replaced by Gd-5d orbitals. The

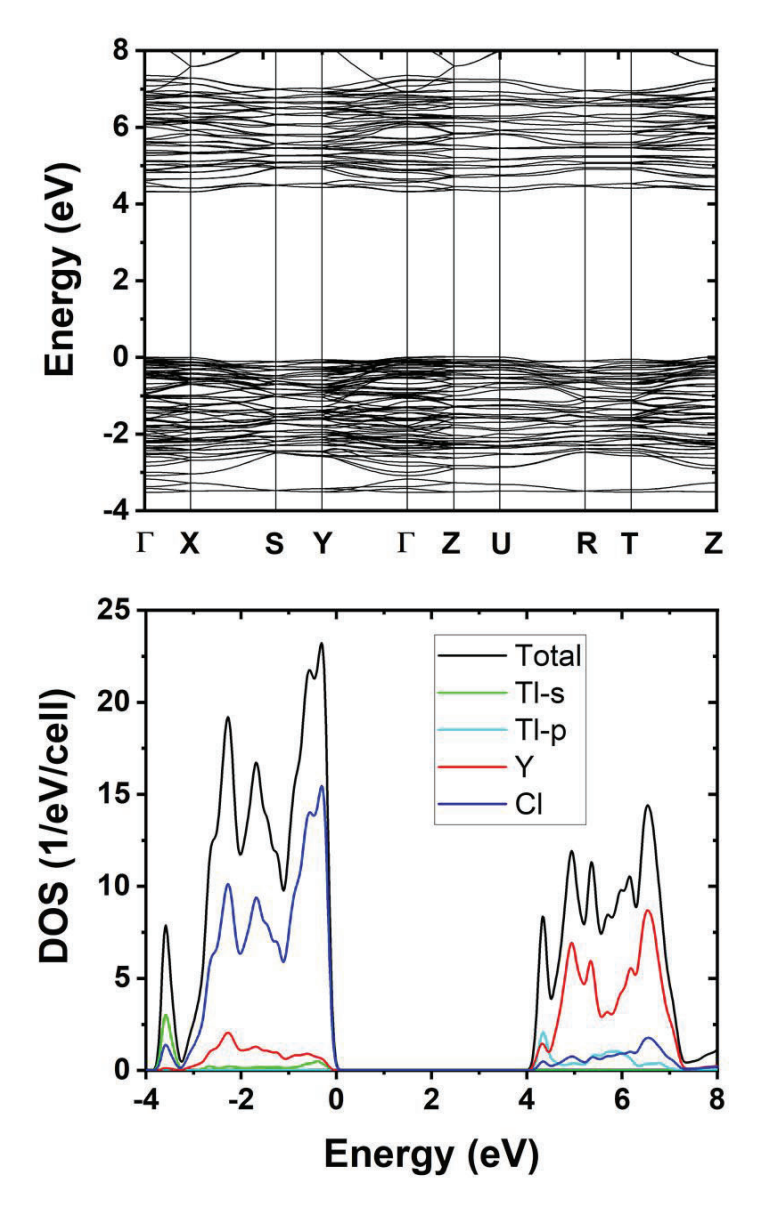


Figure 7. (a) Electronic band structure and (b) density of states (DOS) of TlY₂Cl₇ calculated at the PBE level. Note that the band gap is underestimated. The energy of the VBM is set to zero.

direct band gap at the Γ point is 6.38 eV calculated using the hybrid PBE0 functional. Including Gd-4f orbitals as valence states is expected to introduce a narrow Gd-4f band within the energy gap between Gd-5d and Cl-3p bands.

Tl₃YCl₆ and Tl₃GdCl₆ have a quasi-0D structure, in which YCl₆/GdCl₆ octahedra are separated from each other by Tl ions. The electronic structure and DOS of Tl₃YCl₆ are shown in Figure 8. The band gap is slightly indirect. The CBM is located between Y and X1 points while the VBM is located between X and Γ points. However, both conduction and valence bands have small dispersions. Therefore, the direct band gap at the Γ point (3.73 eV) is only slightly larger than the

indirect band gap of 3.67 eV; both are calculated at the PBE level. The direct band gap is corrected by the hybrid PBE0 calculation to 5.61 eV. Compared to quasi-2D TlY₂Cl₇, the band gap of Tl₃YCl₆ is strongly reduced as can be seen by comparing Figure 7 and Figure 8. The dimensional reduction of the Y-Cl bonding network increases the energy gap between Y-4d and Cl-3p bands. If replacing Tl by Cs, the band gap of Cs₃YCl₆ is expected to be larger than that of CsY₂Cl₇. With the presence of Tl, the conduction band of Tl₃YCl₆ is mainly made up of Tl-6p orbitals, resulting in a relatively small band gap. The same trend is also found in Tl₃GdCl₆. The PBE0 direct band gap at the Γ point is 5.55 eV in Tl₃GdCl₆, strongly reduced from that of TlGd₂Cl₇ (6.49 eV).

268

269

270

271

272

273

274

275

276

277

278

279

280

281

282

283

284

285

286

287

288

289

290

291

292

293

294

295

296

297

298

299

300

301

302

303

304

305

306

307

308309

310

311

312

313

Ce doping inserts both Ce-4f and Ce-5d levels inside the band gaps of TlY₂Cl₇ and TlGd₂Cl₇. The calculated Ce³⁺ emission energies in TlY₂Cl₇ and TlGd₂Cl₇ are nearly identical at 3.31 eV, compared to the experimental values of 3.14 (395 nm) and 3.00 eV (412 nm), respectively. The calculated and measured Ce³⁺-emission energies in TlY₂Cl₇:Ce³⁺ are in good agreement. The somewhat larger difference emission in TlGd₂Cl₇:Ce³⁺ may be related to the missing Gd-4f states in calculation.

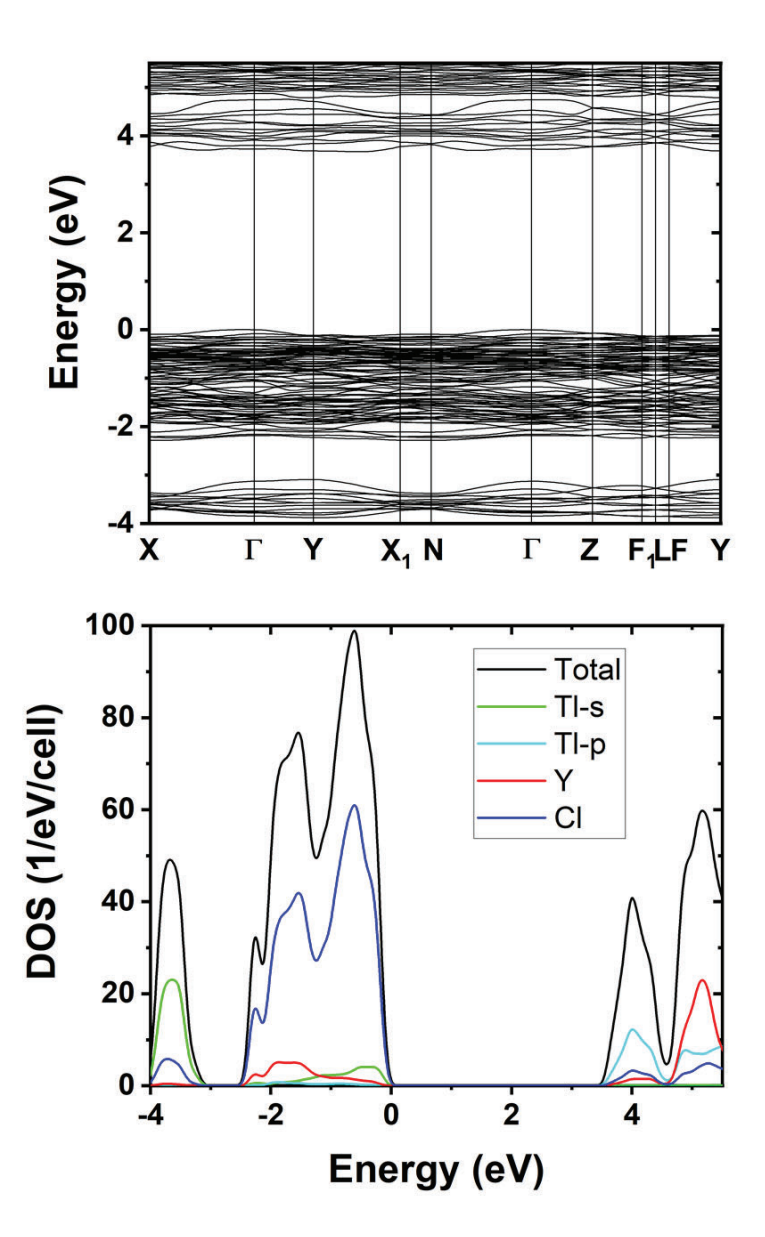


Figure 8. (a) Electronic band structure and (b) density of states (DOS) of Tl₃YCl₆ calculated at the PBE level. Note that the band gap is underestimated. The energy of the VBM is set to zero.

As discussed above, the band gaps of Tl₃YCl₆ and Tl₃YGdCl₆ are strongly reduced from those of TlY₂Cl₇ and TlGd₂Cl₇, respectively, and the reduction is mainly due to the lower conduction bands derived mostly from Tl-6p orbitals. This causes a problem for Ce activation. The Ce-5d and Tl-6p orbitals are close in energy and PBE0 calculations are unable to localize an electron at the Ce-5d level in both Tl₃YCl₆ and Tl₃GdCl₆. Thus, in these two compounds, the intrinsic exciton emission and Ce³⁺ emission may compete and the closeness of the Ce-5d level to the CBM could also lead to electron detrapping and migration, leading to the subsequent energy loss to defects.

3.4 Optical and Scintillation Properties

314

315

316

317

318 319

320

321

322

323

324 325

326

327

328

329

330

331

332

333

334 335

336 337

338

339

340

341

342

343

The X-rav excited radioluminescence spectra TlY₂Cl₇:Ce³⁺, TlGd₂Cl₇:Ce³⁺, and Tl₃GdCl₆:Ce³⁺ are shown in Figure The emission spectra of TIY₂Cl₇:Ce³⁺ and TlGd₂Cl₇:Ce³⁺ show a broad emission band peaking at 395 and 412 nm, respectively, which is attributed to Ce^{3+} 5d \rightarrow 4f emission. Note that there is only a slight difference in the peak emission maximum between the yttriumand gadolinium-based Phyllohalide, possible due to the presence of Gd-4f states (see section 3.3) which are absent in yttrium.

radioluminescence The spectrum of Tl₃GdCl₆:Ce³⁺ is very

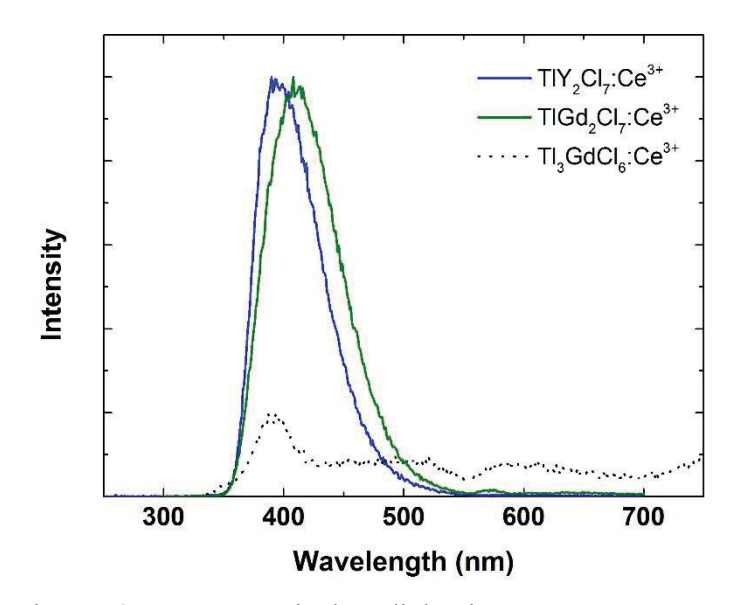
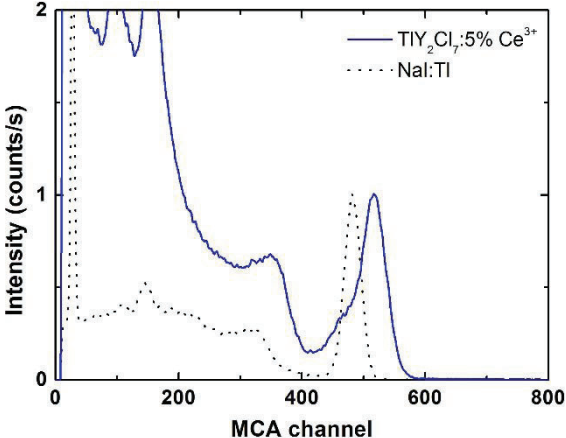
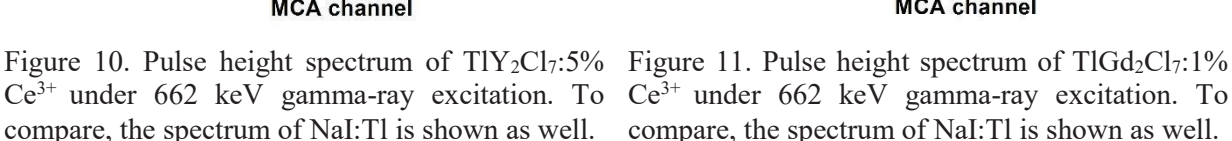


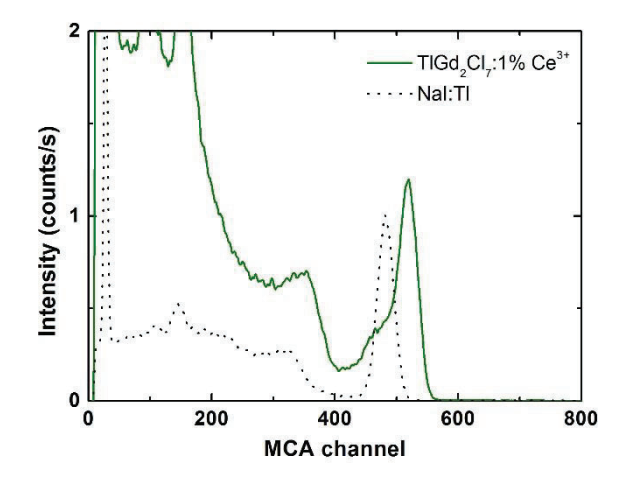
Figure 9. X-ray excited radioluminescence spectra of $Tl_3GdCl_6:Ce^{3+}$, $TlGd_2Cl_7:Ce^{3+}$, and $TlY_2Cl_7:Ce^{3+}$.

weak and noisy, with a potential emission maximum at about 390 nm. We attribute this to the poor crystalline quality of Tl₃GdCl₆:Ce³⁺ as discussed earlier in the crystal growth section of this paper.

The pulse height spectra of TlY₂Cl₇:5% Ce³⁺ and TlGd₂Cl₇:1% Ce³⁺ under ¹³⁷Cs 662 keV gamma-ray irradiation obtained with a shaping time of 4 µs are shown in Figure 10 and Figure 11, respectively (these two crystals were randomly chosen from a larger set). The shoulder to the left of the main photopeak in each pulse height spectrum is attributed to the X-ray escape peak of thallium (at 590 keV). Using a two-Gaussian fit of the photopeak and this shoulder gives us an energy resolution of 9 and 7% (FWHM) at 662 keV for TlY₂Cl₇:5% Ce³⁺ and TlGd₂Cl₇:1% Ce³⁺. respectively. We estimate the light yield of TlY₂Cl₇:5% Ce³⁺ and TlGd₂Cl₇:1% Ce³⁺ to be about 38,000 and 40,000 ph/MeV, respectively. TlY₂Cl₇:5% Ce³⁺ and TlGd₂Cl₇:1% Ce³⁺ are not very







compare, the spectrum of NaI:Tl is shown as well. compare, the spectrum of NaI:Tl is shown as well.

proportional having a deviation from linearity of about 8% (relative to the light yield at 662 keV) at 60 keV (²⁴¹Am source) which contributed to the mediocre energy resolution at 662 keV of both scintillators.

Scintillation decay time spectra of TlY₂Cl₇:5% Ce³⁺ and TlGd₂Cl₇:1% Ce³⁺ are shown in Figure 12.

The obtained decay curves were fitted with a three-component exponential decay function. The short decay component of TlY₂Cl₇:5% Ce³⁺ has a lifetime of about 95 ns and contributes about 48% to the total light yield, whereas the intermediate and longer decay components of 422 and 1.2 µs, respectively, contribute 36 and 16%, respectively. The scintillation decay of TlGd₂Cl₇:1% Ce³⁺ is slightly faster with the short decay component

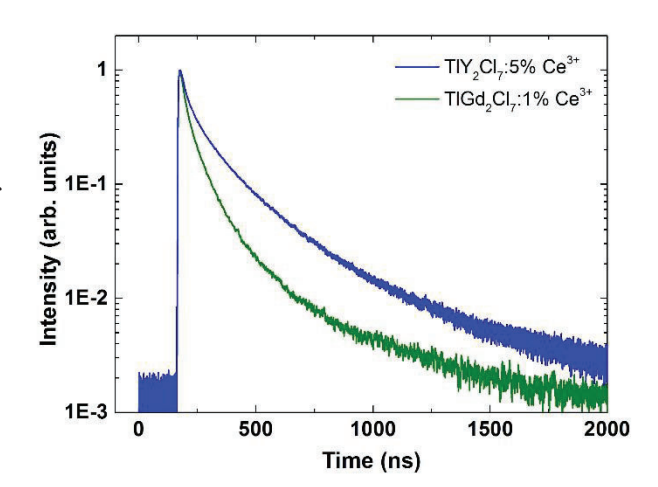


Figure 12. Scintillation decay time spectra of TlY₂Cl₇:5% Ce³⁺and TlGd₂Cl₇:1% Ce³⁺ under 662 keV gamma-ray excitation.

having a lifetime of about 24 ns and contributing about 28% to the total light yield. The intermediate and longer decay components of 87 and 364 ns, respectively, contribute 54 and 28%, respectively.

We attribute the short decay component of each curve to direct capture of electrons and holes at Ce³⁺ as the lifetime of this decay component is of the order of the intrinsic Ce³⁺ decay time. However, at this time we can only speculate about the scintillation mechanism responsible for the intermediate and longer decay components. It could either be energy transfer by binary electronhole diffusion [31] and/or energy transfer by self-trapped exciton (STE) diffusion [32]. More measurements will be needed to confirm or discard either hypothesis.

4. CONCLUSION

In this paper we reported on the crystal growth, density functional theory (DFT) calculations and scintillation properties of $Tl_3LnCl_6:Ce^{3+}$ and $TlLn_2Cl_7:Ce^{3+}$ (Ln = Y, Gd). The scintillators show light yields of up to 40,000 photons/MeV and a gamma-ray energy resolution of 7 - 9% (FWHM) at 662 keV. Density Functional Theory calculations show that the Ce^{3+} energy levels are inside the bandgap. The calculated emission wavelengths are in reasonable agreement with the experimentally determined values.

Due to the poor quality of Tl₃YCl₆:Ce³⁺ and Tl₃GdCl₆:Ce³⁺, and the layered crystal structures and low densities of TlY₂Cl₇:Ce³⁺ and TlGd₂Cl₇:Ce³⁺, we believe that scale-up to industrial sizes will be uneconomic and that these materials are primarily of scientific interest.

5. ACKNOWLEDGEMENT

Powder X-Ray Diffraction was performed at the Joint Institute for Advanced Materials (JIAM) Diffraction Facility, located at the University of Tennessee, Knoxville.

This research was sponsored by the Department of the Defense, Defense Threat Reduction Agency of the United States under grant award no. HDTRA1-19-1-0014. The content of this paper does not necessarily reflect the position or the policy of the federal government, and no official endorsement should be inferred.

- [1] R. Blachnik, E. Enninga," Thermochemische Untersuchungen an Mischungen einiger Lanthanoidchloride mit CuCI, AgCl und TlCl", Z. anorg. allg. Chemie 503 (1983) 133.
- [2] R. Král, P. Zemenová, V. Vaněček, A. Bystřický, M. Kohoutková, V. Jarý, S. Kodama, S. Kurosawa, Y. Yokota, A. Yoshikawa, M. Nikl, "*Thermal analysis of cesium hafnium chloride using DSC–TG under vacuum, nitrogen atmosphere, and in enclosed system,*" J. Therm. Anal. Calorim. (2019) 1-9.
- [3] T. Degen, M. Sadki, E. Bron, U. König, and G. Nénert, "*The HighScore suite*", Powder Diffraction 29 (2014) S13-S18.
- [4] B. H. Toby and R. B. Von Dreele, "GSASII: the genesis of a modern open-source all-purpose crystallography software packaged", J. Appl. Crystall. 46 (2013) 544-549.
- [5] G. Meyer, P. Ax, A. Cromm, H. Linzmeier, "Seven-coordinate trivalent rare earths: the phyllochlorides ARE2Cl7 (A = K, Rb, Cs; RE = Sm Lu, Y) and the crystal structure of InY2Cl7", Journal of the Less Common Metals, 98 (1984), 323-337.
- [6] G. Kresse, J. Furthmüller, "Efficiency of ab-initio total energy calculations for metals and semiconductors using a plane-wave basis set", Comp. Mat. Sci. 6 (1996) 15-50.
- [7] G. Kresse, D. Joubert, "From ultrasoft pseudopotentials to the projector augmented-wave method", Phys. Rev. B 59 (1999) 1758.
- [8] J. P. Perdew, K. Burke, M. Ernzerhof, "Generalized gradient approximation made simple", Phys. Rev. Let. 77 (1996), 3865-3868.
- [9] J. P. Perdew, M. Emzerhof, K. Burke, "Rationale for mixing exact exchange with density functional approximations", J. Chem. Phys. 105 (1996) 9982-9985.
- [10] J. Paier, M. Marsman, K. Hummer, G. Kresse, I. C. Gerber, J. G. Angyan, "Screened hybrid density functionals applied to solids", J. Chem. Phys. 124 (2006).
- [11] A. J. Garza, G. E. Scuseria, "Predicting Band Gaps with Hybrid Density Functionals", J. Phys. Chem. Let. 7 (2016) 4165-4170.
- [12] K. Biswas, M.-H. Du, "Energy transport and scintillation of cerium-doped elpasolite Cs₂LiYCl₆: Hybrid density functional calculations", Phys. Rev. B 86 (2012) 014102.
- [13] M.-H. Du, S. B. Zhang, "Impurity-bound small polarons in ZnO: Hybrid density functional calculations", Phys. Rev. B 80 (2009) 115217.
- [14] A. Janotti, J. B. Varley, M. Choi, C. G. van de Walle, "Vacancies and small polarons in SrTiO₃", Phys. Rev. B 90 (2014), 085202.
- [15] A. Janotti, C. Franchini, J. B. Varley, G. Kresse, C. G. van de Walle, "Dual behavior of excess electrons in rutile TiO₂", phys. stat. sol. (RRL) Rapid Research Letters 7 (2013) 199-203.
- [16] L. Bjaalie, D. G. Ouellette, P. Moetakef, T. A. Cain, A. Janotti, B. Himmetoglu, S. J. Allen, S. Stemmer, C. G. v.d. Walle, "Small hole polarons in rare-earth titanates", Appl. Phys. Let. 106 (2015) 232103.
- [17] J. M. Farmer, L. A. Boatner, B. C. Chakoumakos, M.-H, Du, M. J. Lance, C. J. Rawn, J. C. Bryan, "Structural and crystal chemical properties of rare-earth titanate pyrochlores," J. Alloys Comp. 605 (2014) 63-70.
- [18] J. Xing, L. D. Sanjeewa, J. Kim, G. R. Stewart, M.-H. Du, F. A. Reboredo, R. Custelcean, A. S. Sefat, "Crystal Synthesis and Frustrated Magnetism in Triangular Lattice CsRESe₂ (RE = La–Lu): Quantum Spin Liquid Candidates CsCeSe₂ and CsYbSe₂", ACS Materials Letters 2 (2020) 71-75.
- [19] S. R. Dunsiger, A. Aczel, C. Arguello, H. Dabkowska, A. Dabkowski, M.-H. Du, T. Goko, B. Javanparast, T. Lin, F. L. Ning, H. M. L. Noad, D. J. Singh, T. J. Williams, Y. J. Uemura, M. J. P. Gingras, G. M. Luke, "Spin Ice: Magnetic Excitations without Monopole Signatures Using Muon Spin Rotation", Phys. Rev. Let. 107 (2011) 207207.
- [20] S. Grimme, J. Antony, S. Ehrlich, H. Krieg, H., "A consistent and accurate ab initio parametrization of density functional dispersion correction (DFT-D) for the 94 elements H-Pu", J. Chem. Phys. 132 (2010) 154104.

- [21] R. O. Jones, O. Gunnarsson, "The density functional formalism, its applications and prospects", Rev. Mod. Phys. 61 (1989) 689-746.
- [22] A. Görling, "Density-functional theory beyond the Hohenberg-Kohn theorem", Phys. Rev. A 59 (1999) 3359-3374.
- [23] A. Hellman, B. Razaznejad, B. I. Lundqvist, "Potential-energy surfaces for excited states in extended systems", J. Chem. Phys. 120 (2004) 4593-4602.
- [24] C. Zhou, H. Lin, Q. He, L. Xu, M. Worku, M. Chaaban, S. Lee, X. Shi, M.-H. Du, B. Ma, "Low dimensional metal halide perovskites and hybrids", Mat. Sci. Eng.: R: Reports 137 (2019) 38-65.
- [25] M.-H. Du, "Microscopic origin of multiple exciton emission in low-dimensional lead halide perovskites", J. Chem. Phys. 151 (2019) 181101.
- [26] M.-H. Du, "Emission Trend of Multiple Self-Trapped Excitons in Luminescent 1D Copper Halides", ACS Energy Letters 5 (2020) 464-469.
- [27] D. Han, H. Shi, W. Ming, C. Zhou, B. Ma, B. Saparov, Y.-Z. Ma, S. Chen, M.-H. Du, "Unraveling luminescence mechanisms in zero-dimensional halide perovskites", J. Mat. Chem. C 6 (2018) 6398-6405.
- [28] H. Shi, D. Han, S. Chen, M.-H. Du, "Impact of metal ns2 lone pair on luminescence quantum efficiency in low-dimensional halide perovskites", Phys. Rev. Mat. 3 (2019) 034604.
- [29] M. Loyd, A. Lindsey, M. Patel, M. Koschan, C. L. Melcher, and M. Zhuravleva, "*Crystal structure and thermal expansion of CsCaI*₃: *Eu and CsSrBr*₃: *Eu scintillators*," J. Crystal Growth 481 (2018) 35-39.
- [30] A. C. Lindsey, M. Loyd, M. K. Patel, R. Rawl, H. Zhou, M. Koschan, C. L. Melcher, M. Zhuravleva, "Determination of thermal expansion of KCaI₃ using in-situ high temperature powder X-ray diffraction," Mat. Chem. Phys. 212 (2018) 161-166.
- [31] H. W. Leverenz, "An Introduction to Luminescence in Solids," in: Structure and Matter Series, Wiley, London, 1950, p. 270.
- [32] K. Tanimura, N. Itoh, "The hopping motion of the self-trapped exciton in NaCl," J. Phys. Chem. Sol. 42 (1981) 901 910.